KINEMATICS OF THE MOLECULAR HYDROGEN FROM THE PLANETARY NEBULA NGC 2346[1]

L. ARIAS,[2] M. ROSADO,[2] L. SALAS,[3] AND I. CRUZ-GONZÁLEZ[2]

ABSTRACT

We present scanning Fabry-Perot observations of the planetary nebula NGC 2346 at the near-infrared vibrationally excited line H_2 $S(1)$ 1–0 at 2.122 μm. The kinematics matches a model of two ellipsoids with an outflow velocity proportional to the distance of the gas from the central star and moving radially outward. The stronger emission is located in an equatorial torus expanding at 16 km s^{-1}. It is likely that a shock between 6 and 16 km s^{-1}, depending on the assumed velocity of the red giant envelope (0 to 10 km s^{-1}), excites the molecular gas. Depending on those limiting values for the shock velocity, the density of the preshock gas falls in the range $(0.3–1.7) \times 10^4$ cm^{-3}, and consequently the mass of the molecular gas in the nebula is estimated to be between 0.34 and 1.85 $M_\odot$, much larger than the mass of the ionized gas, and marginally in agreement with the estimate coming from CO observations alone.

Key words: ISM: molecules — planetary nebulae: general — planetary nebulae: individual (NGC 2346)

1. INTRODUCTION

Molecular hydrogen was first detected for a planetary nebula (PN) in NGC 7027 (Treffers et al. 1976), and in the last years, with the ability of new infrared detectors, the presence of this emission has been confirmed in more than 40 PNs. A list of detected and searched but undetected PNs is presented in Kastner et al. (1996). For NGC 2346, molecular hydrogen was first detected by Zuckerman & Gatley (1988), who mapped the 2.122 μm $S(1)$ 1–0 transition, and later it was imaged by Kastner et al. (1994, 1996) and Latter et al. (1995). CO gas has also been detected and mapped (Knapp 1986). NGC 2346 (PK 15+3°1) is a PN with a binary stellar system at the center, composed of an A5 star (Méndez 1978) and a hot companion, which has not been directly observed but its presence is inferred from the high excitation of the nebula. In optical emission, this nebula has a classical bipolar morphology with a narrow central waist containing several bright knots and two filamentary lobes of similar size. It has been classified by Balick (1987) as butterfly, of middle type, with open ends. The total extent and the closed shape of the lobes were shown for the first time in a deep Hα + [N II] image by Walsh, Meaburn, & Whitehead (1991). The overall dimensions of the optical nebula are 3.1 × 0.75, equivalent to 0.6 × 0.15 pc at a distance of 690 pc (Terzian 1997), which will be assumed in this paper.

According to hydrodynamical models, bipolar PNs are the result of a nonuniform distribution of material ejected by the central star while it passes by the asymptotic giant branch. A high equator-to-pole density contrast of the material makes it easier for the gas to flow in the direction of the poles, thus forming the extended lobes. In general, the models reproduce very well the spectral observations; however, most of the work has been done for the ionized gas. Consequently, the structure and kinematics of the molecular gas and the interaction with the atomic gas remain to be studied. The emission of the molecular gas in

NGC 2346 matches remarkably well the optical shape of the nebula and shows two maxima on both sides, east and west from the central star, suggesting that the molecular gas is concentrated in a kind of ring or torus surrounding the star. Previous kinematical studies of NGC 2346 have been made for the ionized (Walsh 1983; Anandarao et al. 1988; Walsh et al. 1991) and the CO molecular gas (Healy & Huggins 1988; Bachiller et al. 1989), and recently Kastner & Gatley (2000) have presented high-resolution long-slit spectra for the H$_2$ emission.

For the H$_2$ gas, two types of mechanisms can populate the upper levels of the transitions arising from excited vibrational-rotational states: (*a*) shock excitation (e.g., Kwan 1977; Shull & Hollenbach 1978) or (*b*) radiative cascades following the UV pumping in photodissociation regions (PDRs) (e.g., Black & van Dishoeck 1987; Sternberg & Dalgarno 1989). These mechanisms result from very different conditions and can, in principle, be distinguished by examining the relative intensities among the different transitions. In particular, it is common to use the ratio $R(2–1/1–0)$ of the 2.248 μm $S(1)$ 2–1 to the 2.122 μm $S(1)$ 1–0 lines. The observed ratio $R(2–1/1–0)$ is typically 0.1 in shocked regions and tends to a limiting value of $\sim$0.3 for strong shocks. In the case of pure UV fluorescence, the ratio $R(2–1/1–0)$ is expected to be $\sim$0.5. However, it has been pointed out that in dense PDRs ($\geq 10^5$ cm^{-3}) thermal collisions push the gas toward an LTE and the $R(2–1/1–0)$ value resembles the one obtained for shocked regions. To avoid this confusion, Takami et al. (2000) have proposed the discrimination of the excitation mechanism by making use of intensity ratios of high vibrational lines. They have suggested that the ratio 1.312 μm $S(1)$ 4–2/1.233 μm $S(1)$ 3–1 discriminates the H$_2$ excitation mechanism more clearly than the $R(2–1/1–0)$ ratio. Nevertheless, whatever excites the molecular hydrogen gas, the mass of the molecular gas could be significant, implying that the average masses of the progenitor stars are higher than previously thought.

In this paper we present new optical direct images of NGC 2346 in the lines of Hα, [N II], [S II] and [O III]. To discriminate between shocks and fluorescence as the excitation mechanism of the H$_2$, images of the nebula in both transitions of molecular hydrogen $S(1)$ 1–0 and $S(1)$ 2–1 are presented. Finally, scanning Fabry-Perot observations of H$_2$ at 2.122 μm allowed us to obtain for the first time the

---

kinematic information for the entire nebula. The observations and data reduction are described in § 2, results are discussed in § 3, and the conclusions are presented in § 4.

2. OBSERVATIONS AND DATA REDUCTION

2.1. Optical Observations

The direct image observations of the planetary nebula NGC 2346 were carried out during the nights of 1998 January 24–25, at the f/7.5 Cassegrain focus of the 2.1 m telescope of the Observatorio Astronómico Nacional at San Pedro Mártir, B.C. (México), using the UNAM Scanning Fabry-Perot Interferometer PUMA (Rosado et al. 1995) in its direct-image mode. A 1024×1024 thinned Tektronix CCD detector, with an image scale of $0\rlap{.}''59$ pixel^{-1}, was used with a 2×2 on-chip binning in both dimensions. Thus, the resulting image format was 512×512 pixels, with a spatial resolution of $1\rlap{.}''18$ pixel^{-1} covering a field of $10' \times 10'$. The images were taken under photometric conditions with a seeing FWHM of $2\rlap{.}''3$. Interference filters were used to isolate the Hα ($\lambda 6563$, $\Delta\lambda = 20$ Å), [N II] ($\lambda 6583$, $\Delta\lambda = 10$ Å), [S II] ($\lambda 6720$, $\Delta\lambda = 20$ Å) and [O III] ($\lambda 5007$, $\Delta\lambda = 10$ Å) emission lines. The exposure time in each filter was 120 s. The data reduction was done in the usual way: bias subtraction and flat-field division.

2.2. Infrared Observations

The infrared images were obtained at the same 2.1 m telescope of the Observatorio Astronómico Nacional at San Pedro Mártir, B.C. (México), using the CAMILA infrared spectrograph (Cruz-González et al. 1994) with a NICMOS3 array (256×256 pixels). The observations were carried out at the f/13.5 Cassegrain focus with a plate scale of $0\rlap{.}''86$ pixel^{-1} covering a field of $3\rlap{.}'6 \times 3\rlap{.}'6$. Direct images under photometric conditions were obtained on 1998 November 2, through narrowband filters for the vibrational transitions of the molecular hydrogen $S(1)$ 1–0 (2.122 μm, $\Delta\lambda = 0.02$ μm) and $S(1)$ 2–1 (2.248 μm, $\Delta\lambda = 0.024$ μm) and also for the continuum at the K band (2.26 μm, $\Delta\lambda = 0.06$ μm). The images were obtained in a "cross" sequence: object, sky to the north, object, sky to the east, object, sky to the west, object, sky to the south, object; each pass had the same exposure time. Total integration times for object and sky were 240 s for each filter. The object frames were each sky-subtracted, by the median of the four sky images, flat-fielded, and then combined. A flux calibration was done by observing faint UKIRT standard stars.

The Fabry-Perot interferometry in the near-infrared (NIR) was carried out by placing a Fabry-Perot interferometer (an ET-50 of Queensgate optimized in the NIR) in the optical bench of the IR spectrograph CAMILA. The main characteristics of this interferometer are interference order of 1181, spectral resolution of 24 km s^{-1}, and free spectral range of 255 km s^{-1}. In this way on 1988 December 8–10 we obtained images in the H$_2$ transition $S(1)$ 1–0 under photometric conditions. The plate scale was the same as in direct images, and the seeing was of $2\rlap{.}''5$ (FWHM). A set of images or a cube was obtained at 26 etalon positions (channels) that scan a single order at 9.82 km s^{-1} channel^{-1}. For more details of the instrumental setup see Salas et al. (1999) and Rosado et al. (1999). Four data cubes were obtained in an observing sequence consisting of alternative imaging, for each spacing gap of the interferometer, of the region, and of a blank sky region $3'$ to the east. The

telescope allowed the on-source image to be accurately positioned back within $1''$, thus eliminating recentering problems. The exposure time was 60 s for each channel. A series of high- and low-illumination sky flats at each etalon position were obtained at sunset for flat-fielding. After sky subtraction and flat-field division for each etalon position, the nebular cubes were co-added to enhance the signal-to-noise ratio (S/N), resulting in total exposure time of 104 minutes. The 2.1332885 μm line (for air) of the Ar lamp was observed at each etalon position for calibration after the source and sky images, obtaining a velocity uncertainty of 0.5 km s^{-1} in the wavelength fit. The data reduction and analysis were performed using the specific reduction package CIGALE (Le Coarer et al. 1993), IRAF tasks, and specially developed FORTRAN programs. These different reduction packages were used to carry out the wavelength calibration of the data cubes to obtain continuum-subtracted λ-cubes (or velocity maps) and to carry out the emission-line profile analysis. All the velocities reported in this paper are heliocentric velocities; to convert them to LSR velocities it is necessary to subtract 16.8 km s^{-1}.

3. RESULTS

3.1. Optical Direct Images

CCD images of NGC 2346 have been shown in the literature (see, for example, Chu, Jacoby & Arendt 1987; Balick 1987). In Balick's images the lobes are partially detected, and it is not possible to see if they are open or not. A deep Hα + [N II] image published by Walsh et al. (1991) shows that the lobes are closed ellipses. However, they show only the image at Hα + [N II]. Our images do not reveal any new structure in the central part of the nebula, but from them we can obtain the shape and the total extent of the lobes at different emission lines and consequently information about the excitation conditions in the lobes. Figure 1a shows a color composite image where red is [N II], green is Hα, and blue is [O III]. The scale is logarithmic and the levels have been chosen to show the structure of the lobes. Figure 1b is similar to 1a but with higher contrast to show in more detail the bright central region, which has the appearance of a tilted ring or torus surrounding the central star. It is evident that the Hα emission is located in the central region. The [O III] emission fills the lobes and is also detected inside the torus. The [N II] is the more extended emission and delineates the outer boundaries of the closed lobes. The central torus is better appreciated by its emission at low-excitation lines. Figure 1c shows the nebula in the [S II] line. For this line, the brightest emission is detected in the central waist and also in several condensations or knots located in both lobes. A faint emission is seen at the ends of the lobes. In all the emission lines shown in Figure 1, the lobes appear closed. The nebular dimensions in the [N II] line (the more extended emission) are $45''$ (0.15 pc) along the equator and $180''$ (0.60 pc) along the polar axis, while the torus has a width of about $15''$ (0.05 pc) at the assumed distance of 690 pc. The position angle of the polar axis is $162°$. The extent and closed shape of the lobes are important features that will be considered below, in the geometric model used to calculate the kinematical and some of the physical parameters.

3.2. Direct Near-Infrared Images

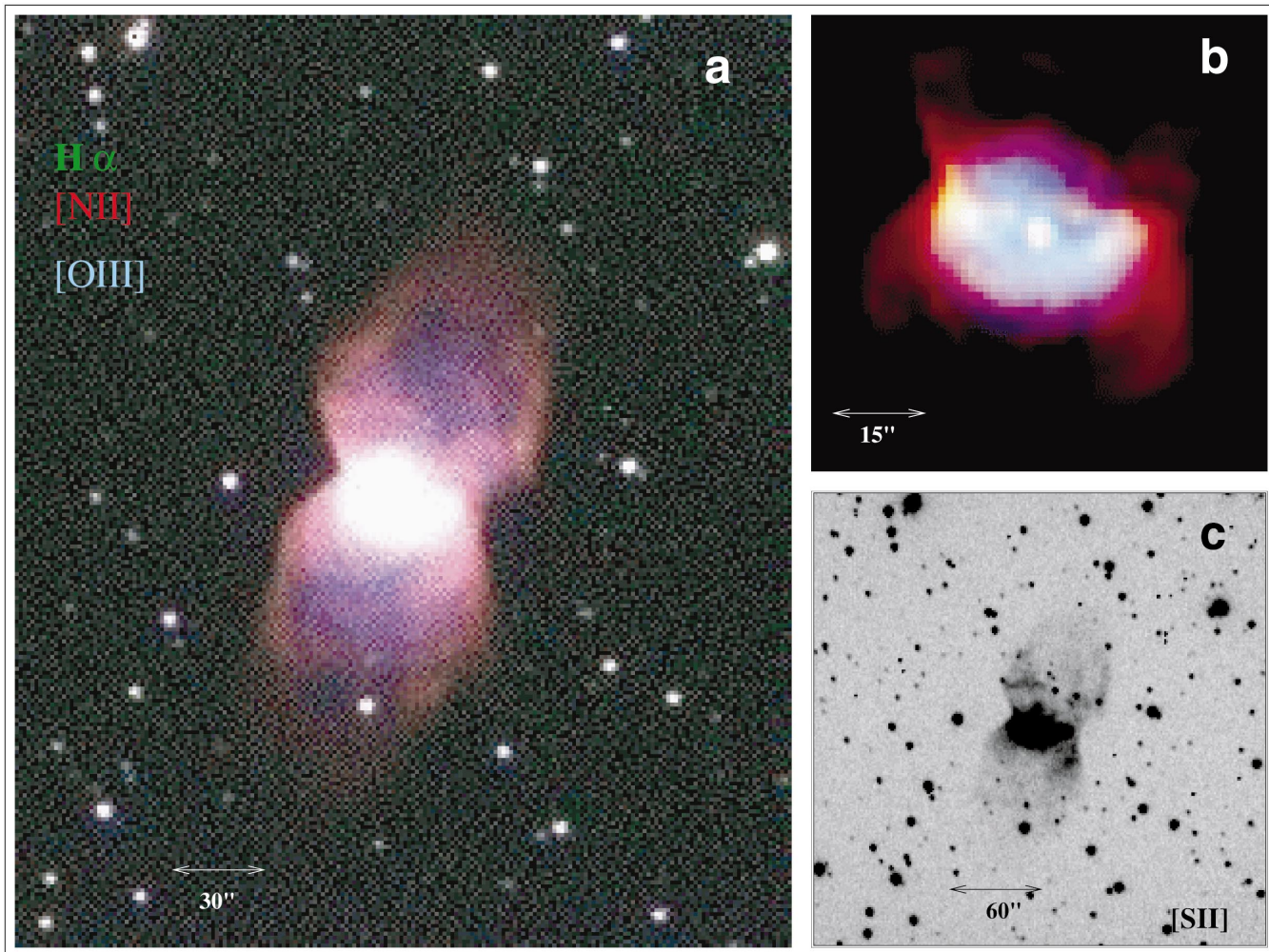In Figure 2 we show direct images of NGC 2346 in the molecular hydrogen emission lines at (a) 2.122 μm, $S(1)$ 1–0

FIG. 1.—(a) Color composite image of the [N II] (λ6583; red), Hα (λ6563; green), and [O III] (λ5007; blue) emission from NGC 2346 in a logarithmic scale. (b) Same as (a), showing the equatorial ring in detail. (c) The nebula in the [S II] (λ6717, 6731) emission lines. A scale bar is shown with each image.

transition; (b) 2.248 μm, S(1) 2–1 transition; and (c) the 2.26 μm continuum at the K band. The emission at 2.122 μm S(1) 1–0 is the brightest. As pointed out by Kastner et al. (1994), the image displays a filamentary structure and the stronger emission lies along the waist and along the edges of the lobes. The S(1) 2–1 emission is weak and is detected basically in the interior of the torus (i.e., in the same location as the [O III] emission). The continuum is weak and has not been subtracted from the emission lines. One of the main results of the H_2 spectrum predicted by fluorescence models (Sternberg & Dalgarno 1989) is the expected value of ~0.5 for the intensity line ratio R(2–1/1–0). Once we have corrected for the bandwidth of the filters and divided the H_2 emission line images, we found that the R(2–1/1–0) line ratio has a maximum value of 0.15, suggesting that the main excitation mechanism is due to shocks rather than fluorescence. However, in more recent models (Natta & Hollenbach 1998) it is shown that the shock contribution is never dominant for typical red giant wind parameters. We will discuss this below.

3.3. Kinematics of the Molecular Gas

From the Fabry-Perot data, we derived a set of velocity maps, shown in Figure 3, for the 2.122 μm line of the H_2. The continuum has not been subtracted so the central star appears in the images. The nebular emission is detected in a wide range of heliocentric velocities from −12 to +66 km s^{-1}. The maximum intensity occurs at +27 km s^{-1}, close to the radial velocity (+25 km s^{-1}) of the central star (Méndez, Niemela, & Lee 1978). The northern lobe predominates at red channels while the southern lobe does at blue channels, as it is expected for a bipolar nebula whose polar axis is tilted relative to the line of sight and the southern lobe closer to the observer. This tilt is also seen in Figure 4, which shows a color-composite image taking three consecutive velocity channels, with $V_{helio} = +17, +27$, and +37 km s^{-1}, around the central velocity as blue, green, and red, respectively. The velocity maps (Fig. 3) reveal clearly the torus surrounding the central star and the presence of knots in the central region, as well as the filamentary structure of the lobes. It can be noted that the back (redshifted) part of the torus is brighter and more homogeneous than the front (blueshifted) part, which seems to be somewhat disrupted. If the equatorial ring is intrinsically circular, the tilt is ~70°.

We have studied the expansion velocity of the emitting molecular hydrogen gas by means of position–radial velocity diagrams (PRVDs) along lines parallel and perpendicular to the polar axis. Each PRVD is equivalent to a long-slit spectrum obtained with a classical spectrograph. Figure 5 shows the nebular image with the fitted ellipsoidal shape for the lobes and also the positions where the PRVDs were
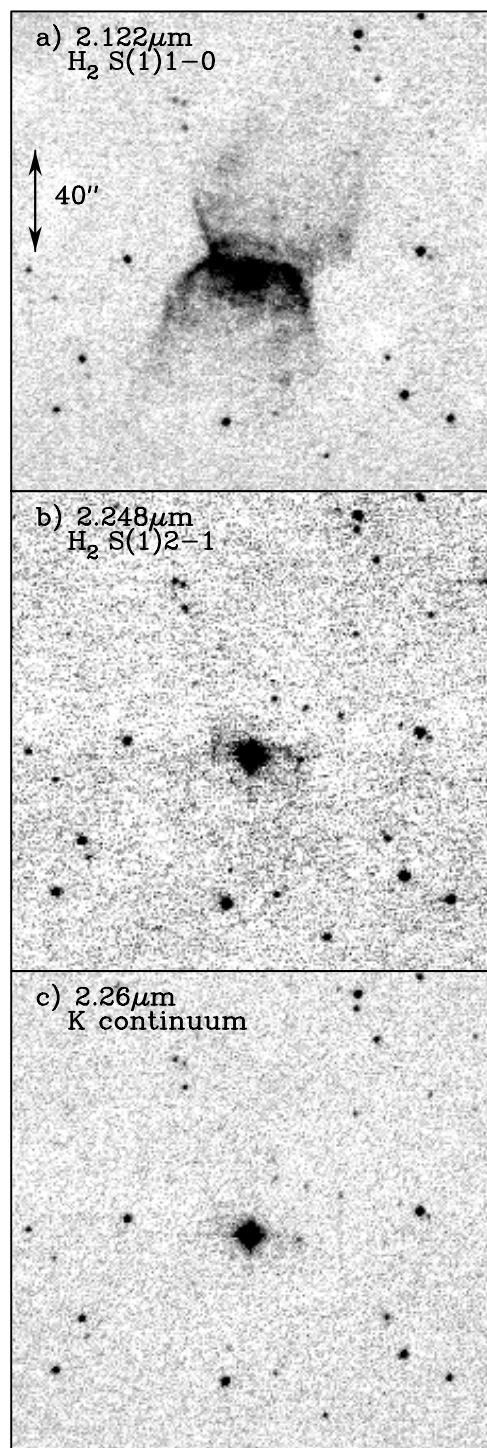
Fig. 2.—NGC 2346 in (a) the 2.122 μm H_2 $S(1)$ 1–0 emission line, (b) the 2.248 μm H_2 $S(1)$ 2–1 emission line, and (c) the 2.26 μm continuum at K band. A 40″ scale bar is shown in (a).

extracted. The PRVDs obtained for these positions are shown in Figure 6. The cuts perpendicular to the long axis (pos4–6) show velocity ellipsoids very similar to those found in the [N II] emission line by Walsh et al. (1991), with velocity differences of about 30 km s^{-1}, which imply an expansion velocity of about 15 km s^{-1} without correcting for inclination effects. For the cut labeled "pos4" (northern lobe) the red component is brighter, while for pos6 (southern lobe) the blue component is the one that is brighter.

This behavior is discussed in § 3.4. Cuts parallel to the polar axis (pos1–3) do not show closed ellipses, but blue and red components in the region close to the star are present.

High-resolution spectra (4 km s^{-1}) of the equatorial region of NGC 2346 have also been presented by Kastner & Gatley (2000). Their slit positions were placed with a different orientation than ours, oriented east-west, instead of perpendicular to the polar axis as in this work. The kinematical features are comparable because the velocity differences also are approximately equal to 30 km s^{-1}. In general, the spectra show two distinct kinematical components: from the torus and from the lobes; however, since these spectra have been obtained near the torus little information can be derived for the lobes. These spectra also agree with the kinematical behavior mentioned before in the sense that the brighter southern part of the torus is redshifted while the brighter northern part is blueshifted.

The velocity profiles integrated over a number of boxes along the position of the cuts have been extracted. In Figure 5 line profiles and the positions over which they were obtained are shown. In most of the extracted line profiles two velocity peaks are present, corresponding to the front and back components of the bipolar cavity. The heliocentric radial velocity of each component has been obtained by a Gaussian profile fitting used to simulate the observed line profiles as a sum of Gaussians, after deconvolution with the Fabry-Perot instrumental function of appropriate height, width, and position. The resulting heliocentric radial velocity of the individual components are plotted in Figure 7, where there exist two components; the brighter one is represented by filled circles.

3.4. Geometric Models

The observational data (morphology and kinematics) are compared with a series of geometric models that also include a velocity law. For this, we use two different geometries: an open biconical structure (Fig. 8a) and two superposed ellipsoidal shells (Fig. 8b). In both cases we assume either a gas moving radially from the central star or moving along the walls of the cavities, with a flow law of the form $V = ar^\alpha$, where r is the distance to the star. To compare the models with our observations, we reproduce PRVDs for each geometry, at different positions in the nebula. At this point we take into account only the morphology and the velocity difference behavior, while the emission intensity of each velocity component is not considered. Figure 9 shows the predicted PRVDs for the two geometric models considered and two different velocity laws for a position along the polar axis. As one can see from this figure, the biconical model predicts PRVDs that are not in agreement with the qualitative behavior of our observed PRVDs, and consequently we discard biconical models. The remaining model parameters are derived as follows: we compared the way the gas is flowing (radially or along the walls) with our data. Our observed PRVDs are more in agreement with a radial flow. Once we have decided on the appropriate geometry and decided that the gas flows radially, we carry out a fine tuning by changing the values of the coefficient α in the flow law and the tilt angle of the bipolar nebula to reproduce the split of the velocity components. In conclusion, we found that the morphology and kinematics match best the model of the two ellipsoids with an outflow velocity $V \propto r$ ($\alpha = 1$) moving radially. However, a very accurate comparision with the observed PRVDs is impossible to obtain because
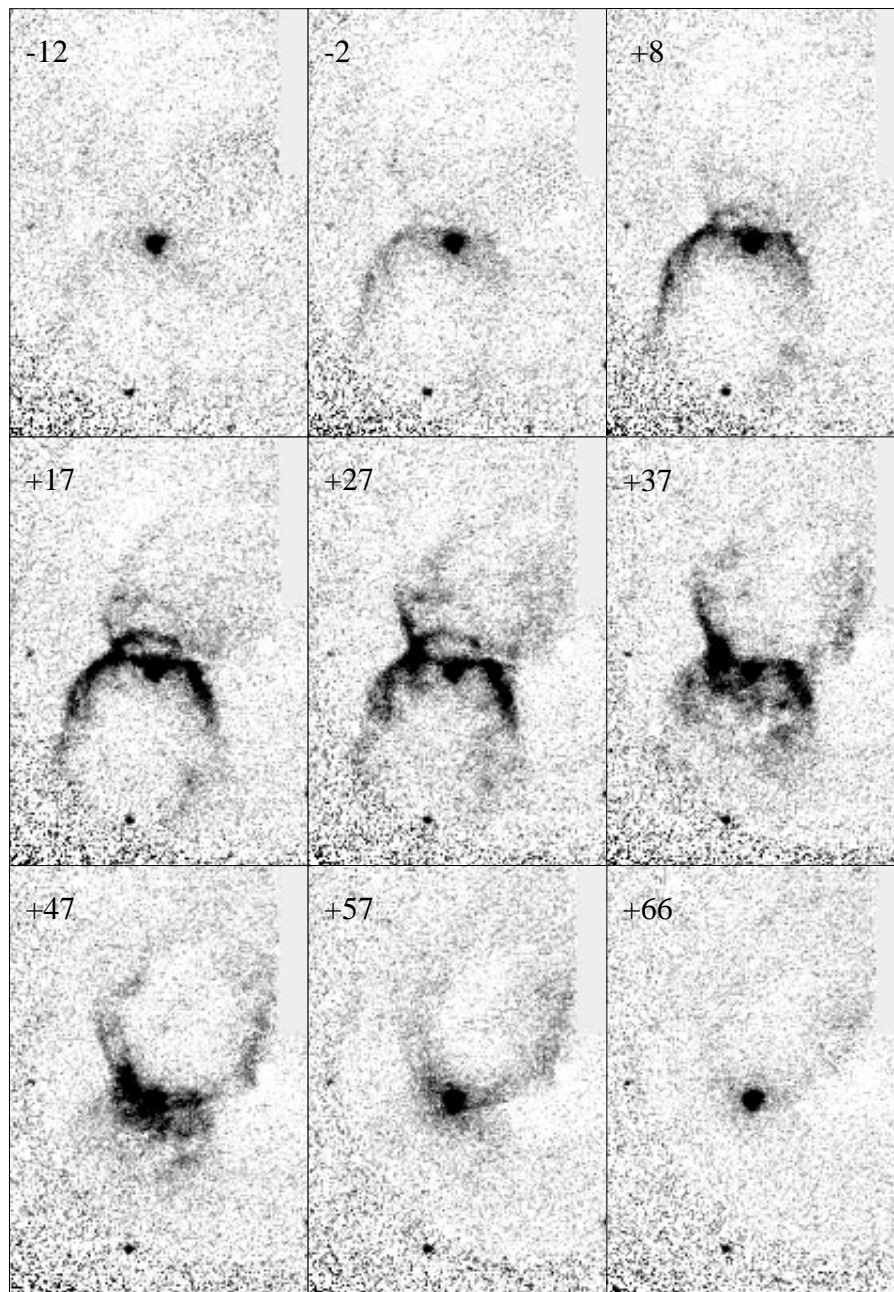
FIG. 3.—Radial velocity maps (λ-channels) of the 2.122 μm H$_2$ $S(1)$ 1–0 emission of NGC 2346. The heliocentric velocity appearing in each frame is in kilometers per second.

the actual nebula is more complicated than our simple idealizations. In this context, we search only for a model that, within our limitations, best reproduces the observed data. Figure 10 shows the predicted PRVDs of one plausible model and the observational data for (a) a cut parallel to the polar axis and (b) a cut perpendicular to the polar axis, indicated by pos3 and pos4, respectively, in Figure 5. For the best match, a tilt of 65° of the polar axis relative to the line of sight is required. Errors involved in the comparisions were estimated by calculating the mean deviation of the observational data from the predicted points. For the best case, the mean error is 6 km s^{-1}. This two-ellipsoid model behavior has been also found for the [N II] line of the ionized gas (Walsh et al. 1991).

Applying this model to the H$_2$ data, the resulting expansion velocity of the gas in the torus is $\sim$16 km s^{-1}, once it is deprojected for the tilt of the nebula, while for the external regions the gas reaches velocities of $\sim$60 km s^{-1}. The velocity values are comparable to those measured for the [N II] ionized gas: the torus is expanding at 12 km s^{-1}, and at the end of the lobes the gas is flowing at 50 km s^{-1}. As the gas is expanding in a red giant medium moving at 0–10 km s^{-1} (this will be considered in more detail in § 3.5), this implies shock velocities of up to $\sim$50 km s^{-1}. Molecular dissociation occurs for J-type shocks faster than 25 km s^{-1}; thus, it is expected that dissociation takes place in these zones and that no molecular emission should be detected in the outer regions of the nebula. In Figure 10 (top), the line
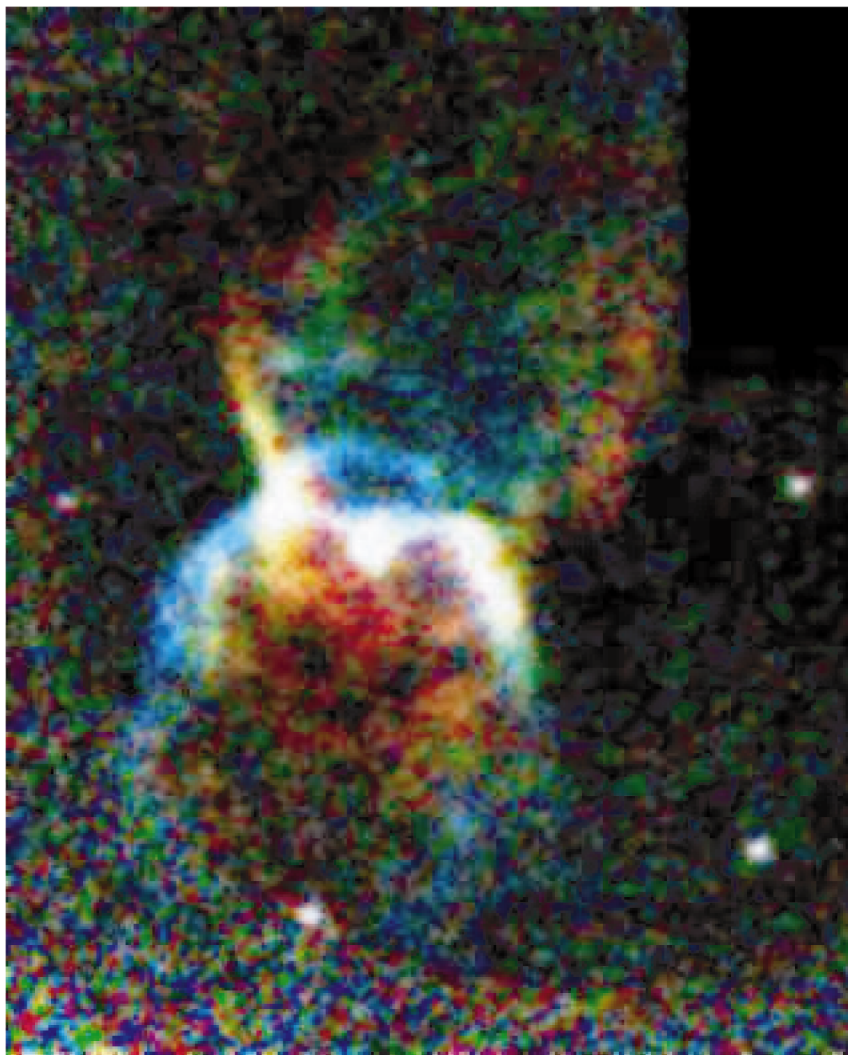
Fig. 4.—Color composite image for NGC 2346 of the H_2 emission, taking three consecutive velocity maps around the central velocity, showing the map at $V_{helio} = +17$ km s^{-1} (*blue*), at $V_{helio} = +27$ km s^{-1} (*green*), and at $V_{helio} = +37$ km s^{-1} (*red*).

corresponding to the predicted PRVDs is continuous for the points where the shock velocity does not exceed the dissociation limit, and a dashed line shows the points where the shock velocity exceeds that limit. The shock velocity is considered the relative velocity of the shell expanding in the moving medium of the ejected red giant envelope. For this plot we have assumed that the red giant envelope is moving at 10 km s^{-1} (this corresponds to the more favorable limiting value as it will be discussed in § 3.5). As one can see, emission is detected far beyond the dissociation limit, thus, if this model holds, that would imply that it is probable that C-type shocks (i.e., with an important magnetic field) are responsible for this emission or that the hydrogen molecule is more robust than previously thought, as recent computations seem to find (Williams 2001).

Another interesting result of our observations is the velocity discontinuity of the brighter component across the polar axis of the nebula: south of the star the more positive velocity component is brighter, while north of the star the more negative component is the brighter one (see Fig. 7), similar to what was found by Walsh (1983) for the [N II] line profiles. While we cannot rule out the possibility that this PN displays point symmetry, other explanations can account for this asymmetry. The difference in intensities

from the approaching and receding regions of the nebula was explained as a difference in volumes subtended along the line of sight per unit solid angle in a biconical walls geometry, with matter uniformly distributed within the walls (Anandarao et al. 1988). Another explanation is a true difference in density of the two components. Because of the inclination of the nebula, the points of the lobes intersected by the line of sight are at different distances from the central star, and if the ellipsoidal shells do not have a uniform density it is reflected in the intensity of the different velocity components. Walsh et al. (1991) show that a variation of the intensity of the [N II] line with radius of the form r^{-2} reproduces well the central bright waist and the faint lobes observed for the ionized gas. Our two-ellipsoid shell model has the bright torus integrated to the ellipsoids. Consequently, we also require a density law to reproduce the differences in brightness between the torus and the lobes. We have tried to derive a density law by calculating the integrated flux of each velocity component by assuming that they result from different distances of the central star due to the tilt of the nebula. However, the S/N ratio of the weak component is too low to derive a reliable density law. Consequently, we have adopted an r^{-2} law for the density based on the shell model calculations of Pascoli (1990) for
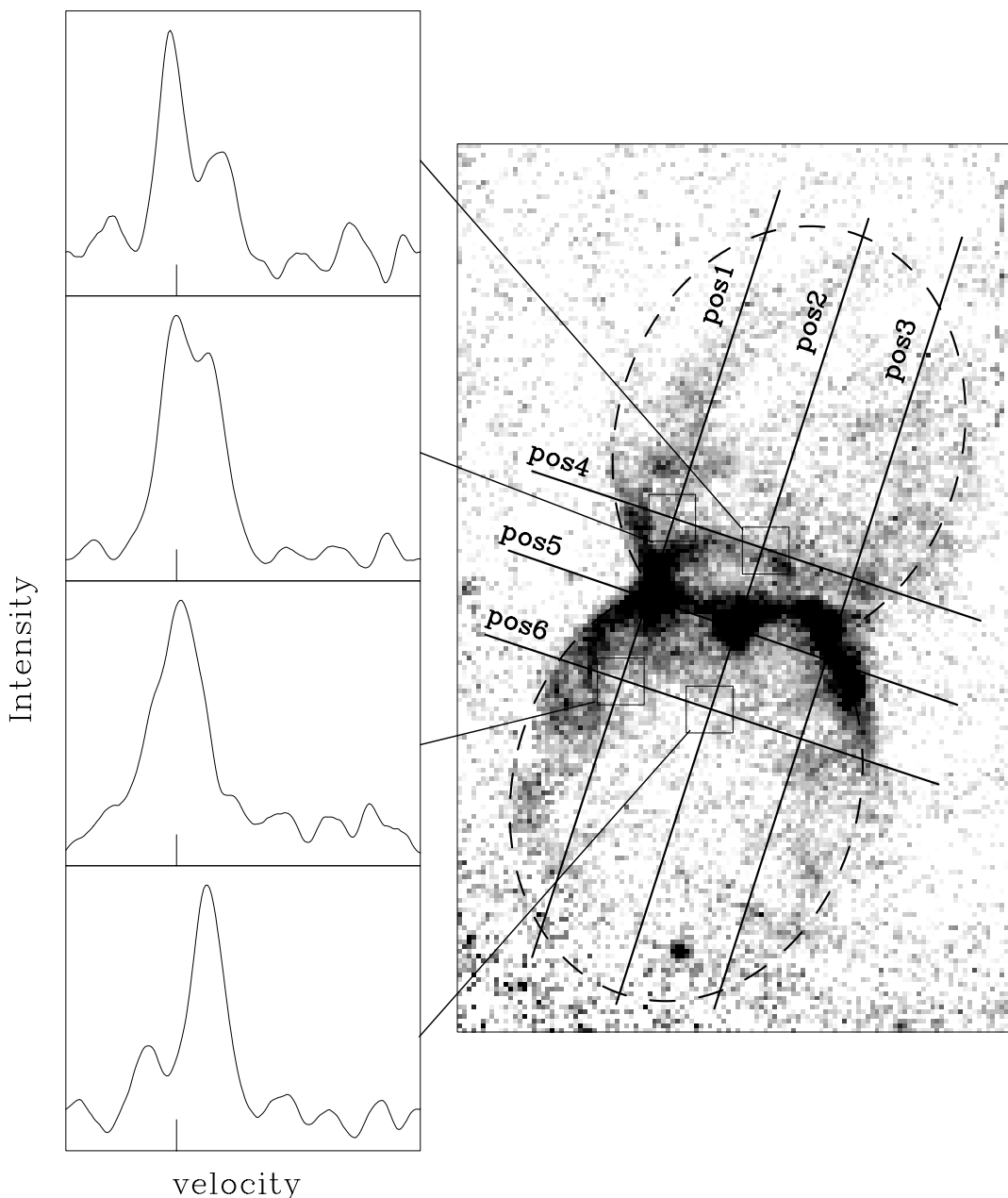
Fig. 5.—Image of NGC 2346 corresponding to the H_2 emission at a heliocentric velocity of $+27$ km s^{-1}, showing the fitted shape of the lobes (*dashed line*), some of the integrated radial velocity profiles, and the regions over which the displayed velocity profiles were obtained (*boxes*). The lines marked with the labels "pos1" to "pos6" indicate the loci of the position-velocity cuts shown in Fig. 6. The mark in the velocity axis corresponds to the systemic heliocentric velocity of the nebula.

PNs that show that the radial dependence of the density is in the form of a power law, $n_e \sim r^{-\beta/2}$ with β between 0 and 2 and the angular latitude density dependence given by Zhang & Kwok (1998) for NGC 2346, in addition to a geometry of two ellipsoids that is close to the $n_e \sim r^{-2}$ case. Furthermore, since the velocity increases linearly with r, an r^{-2} law for the density ensures pressure equilibrium for the gas in the ellipsoidal shells. This is in agreement with the fact that the ellipsoids are still closed. Consequently, the r^{-2} law for the density seems to be a good assumption in this case.

3.5. *Mass of the Molecular Gas*

In this section we propose a method for the mass determination of the molecular gas in the bipolar PN NGC 2346.

This method is compared with a mass determination from CO data. As we will discuss below, both methods are complementary and allow us to limit the values of this important parameter.

3.5.1. *Mass Estimate of the Shocked Molecular Hydrogen*

Taking into account the results of our IR direct images that show that NGC 2346 is more likely excited by shocks, we can use the calibrated direct image at 2.122 μm to estimate the mass of the shocked molecular hydrogen. A previous value has been reported by Zuckerman & Gatley (1988) by mapping the nebula with a 12″.4 beam. Our better spatial resolution allows us to derive a total flux, integrated over the emission in the central waist and the bright limbs of the lobes, of 2.8×10^{-11} ergs cm^{-2} s^{-1}. If the emission is
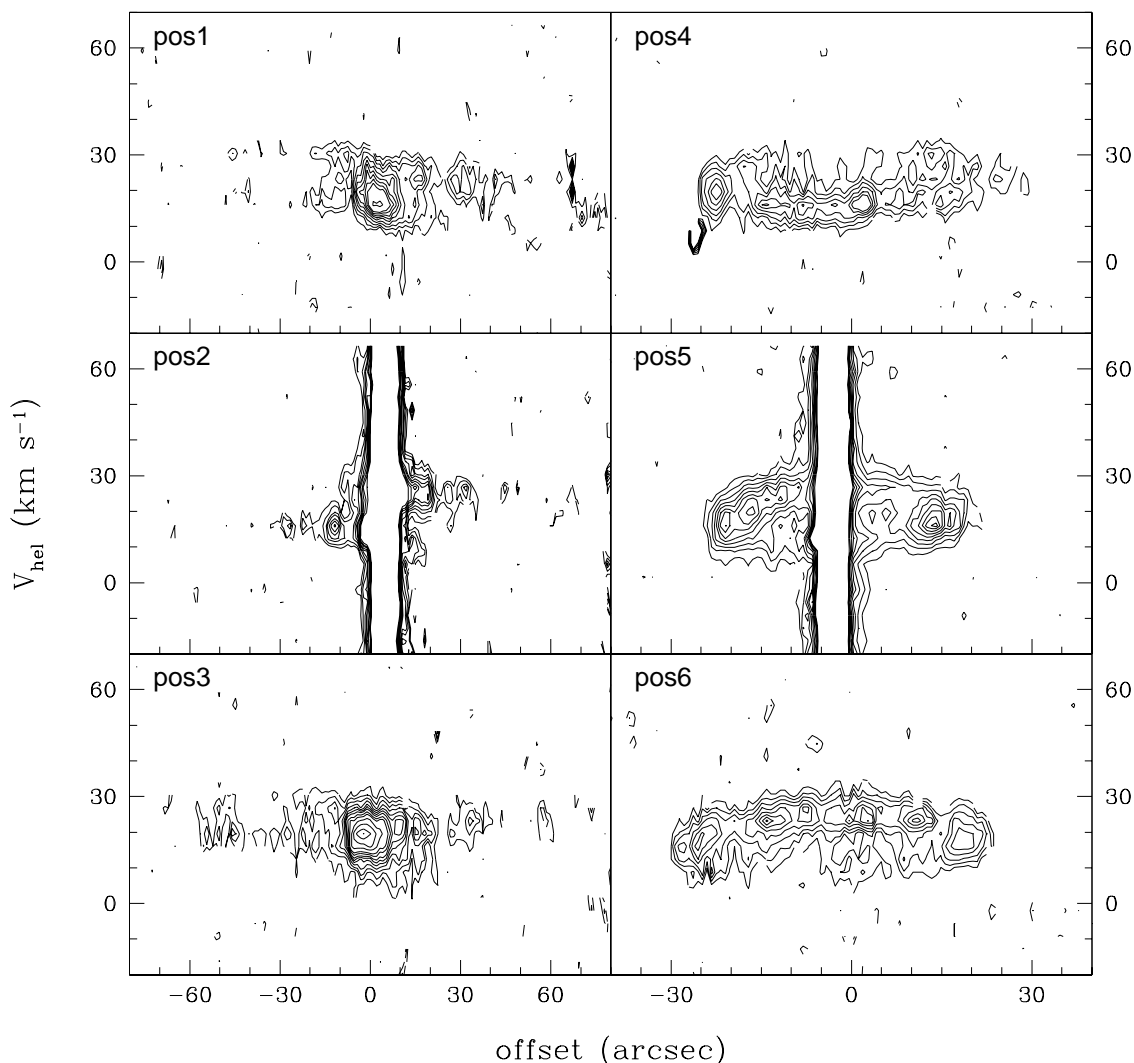
FIG. 6.—Position–radial velocity diagrams obtained for the cuts shown in Fig. 5

due to shocks, as the line ratio $R(2–1/1–0)$ suggests, we can assume a Boltzmann population distribution, and then the mass of the shocked molecular hydrogen, $M(H_2)$, can be obtained by using the relation

$$M(H_2) = \frac{Q(T_{ex})e^{E/kT_{ex}}M_{H_2}F4\pi D^2}{g_J h\nu A},$$

where T_{ex} is the excitation temperature, $Q(T_{ex})$ is the partition function, E is the energy of the upper state, ν is the line frequency, A is the spontaneous emission coefficient, and F is the total line flux at Earth for the source at a distance, D. For $T_{gas} = 2000$ K, which is a typical value for the H_2 gas, and adopting a distance of 690 pc, the mass of hot H_2 shocked gas is 1.29×10^{-4} $M_\odot$. However, the mass of the unshocked molecular H_2 must be much greater because only a thin portion of the torus is shocked.

3.5.2. Mass Estimate of the Molecular Gas in the Torus

To estimate the total mass of the molecular hydrogen (shocked and unshocked) in the torus, we require the torus preshock density. Kwan's (1977) shock models imply a relation between the shock velocity, V_s, the preshock density, n_0, and the intensity of the $S(1)$ 1–0 emission line of the form

$n_0 \sim S_{1-0}V_s^{-1.7}$. If an expanding shell is moving at a velocity V_{sh} through a slow-moving medium such as the red giant's wind, the shock velocity is $V_s = V_{sh} - V_{rg}$, where V_{rg} is the velocity of the red giant's wind.

Usually, the velocities of the CO gas are taken as characteristic of the red giant envelope velocity. In the case of NGC 2346 the CO velocity at the torus is 18 km s^{-1} (Bachiller et al. 1989), very similar to the velocity of the H_2 gas that we report here, so it looks like the CO, the H_2, and the ionized gas move at the same velocity. In the case of the lobes there is no velocity information for the CO. Since there is no direct measurement of the velocity, V_{rg}, in this PN, we assumed three values: $V_{rg} = 0$, 5, and 10 km s^{-1} for the velocity of the red giant wind in the equatorial direction. Thus, using our kinematic data, at the torus V_{sh} is 16 km s^{-1} (see § 3.4) and consequently V_s is 6, 11, or 16 km s^{-1}. The average $S(1–0)$ surface brightness at the central waist is 6.25×10^{-5} ergs s^{-1} cm^{-2} sr^{-1}, and consequently the preshock density, n_0, in that region is $(0.3, 0.7,$ or $1.7) \times 10^4$ cm^{-3}. Only the first value is comparable to the one reported for the CO gas in the torus (Bachiller et al. 1989). Adopting the value of 3×10^3 cm^{-3} would imply that the red giant wind is at rest at least at the equator, which is difficult to understand because the torus has been ejected at some
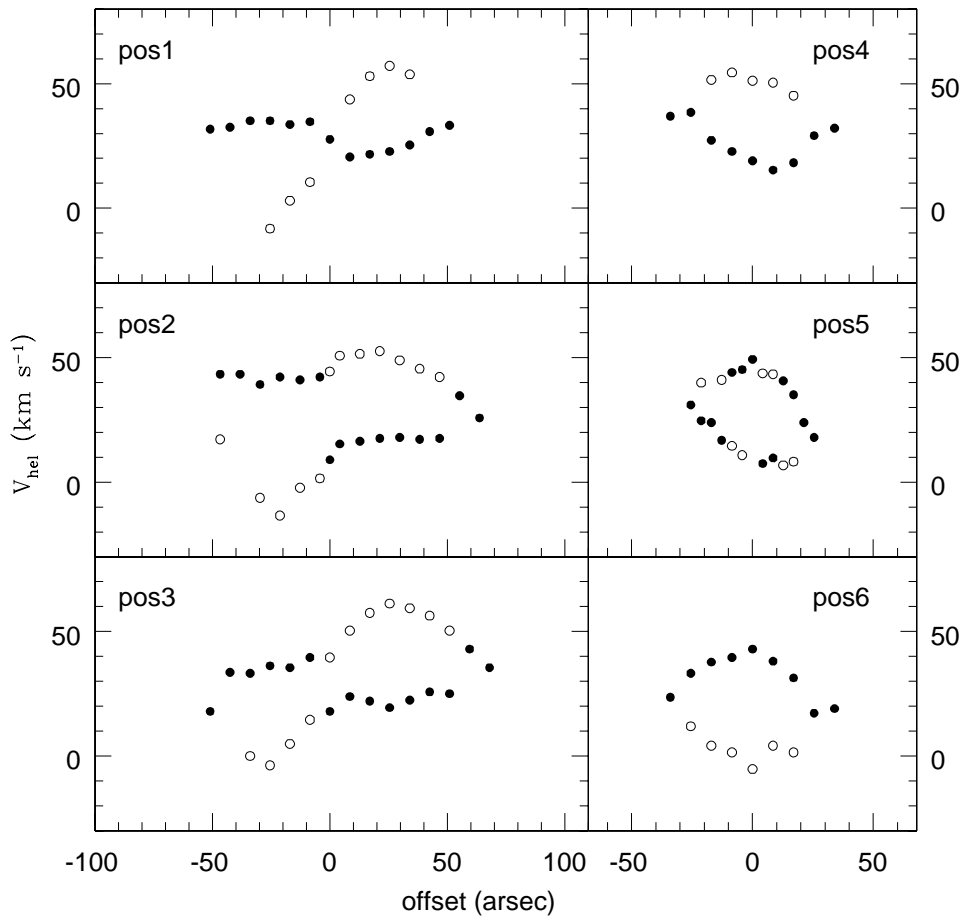
FIG. 7.—Position–radial velocity plot of components found by Gaussian fitting. Profiles that show two velocity components are marked with filled and open circles for the weak and bright components, respectively.

velocity. On the other hand, the value obtained by the CO data represents only a very rough estimate because in CO observations the measured quantity is the column density, which is equally sensitive to changes in density and temperature (also unknown). In that context, a density of 3×10^3 cm^{-3} corresponds to a temperature of about 50 K, which Bachiller et al. (1989) considered reasonable. However, a density of 1.7×10^4 cm^{-3} could also be derived from the same CO observations if we assume a temperature
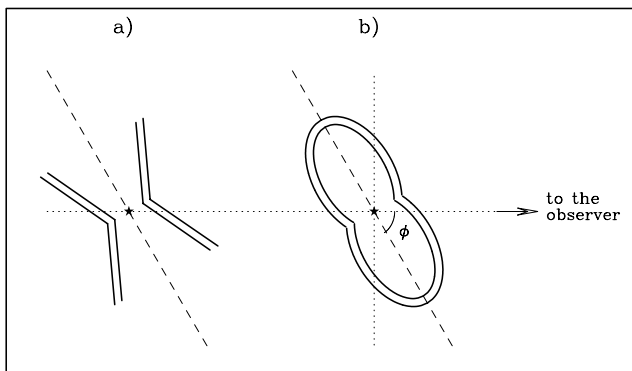

FIG. 8.—Geometric models used to fit the kinematical data: (a) an open biconical structure, (b) two superposed ellipsoidal shells.
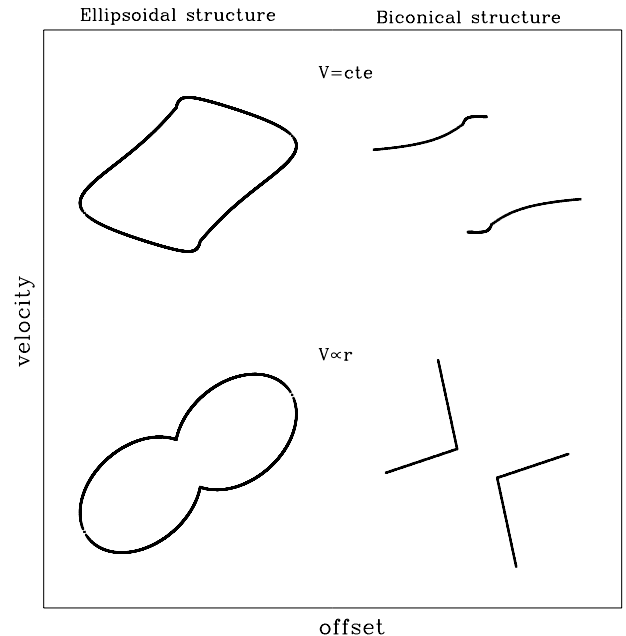

FIG. 9.—Predicted position-velocity plots for the two geometries represented in Fig. 8. The different expansion velocity laws correspond to the case in which the gas is moving radially from the central star.
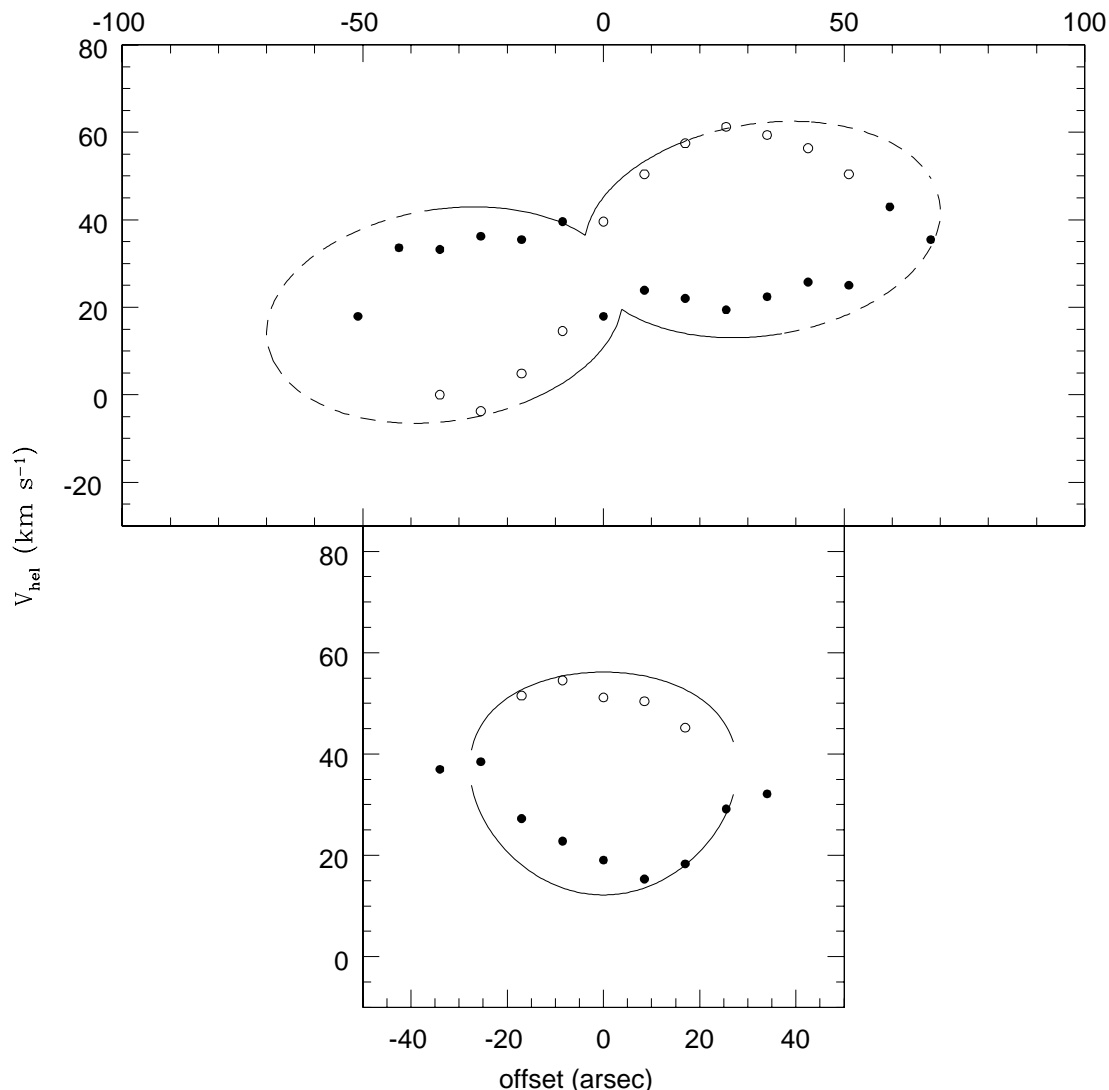
Fig. 10.—Predicted position velocity plots for cuts parallel (*top*) and perpendicular (*bottom*) to the polar axis. The continuous line represents the points where the shock velocity $V_s \leq 25$ km s^{-1} (dissociation limit for the molecular hydrogen), assuming a red giant envelope with $V_{rg} \sim 10$ km s^{-1}. The dashed line corresponds to points that reach $V_s \geq 25$ km s^{-1}. Points represent the observational data with filled and open circles as in Fig. 7.

of about 10 K. It is reasonable to think that the proximity of a very hot star (as the PN nucleus) heats the molecular gas to more than 10 K. Thus we see that there are different reasons for discarding the very limiting values of the pre-shock density (3×10^3 and 1.7×10^4 cm^{-3}). Therefore, the density is more likely an intermediate value such as 7×10^3 cm^{-3}. However, we have shown that the uncertainties of the methods discussed above do not allow us to obtain a more accurate value.

To obtain the mass of the torus, we take a torus of radius 0.06 pc and width 0.033 pc and we assume a constant density equal to $n_0 = 7 \times 10^3$ cm^{-3}. We obtain a torus mass of 0.6 $M_\odot$.

3.5.3. *Total Mass of the Molecular Gas in NGC 2346*

The total H$_2$ mass of the nebula can then be estimated using the morphological model mentioned in § 3.4, assuming both a density law that decreases as r^{-2} and the same red giant wind's values as those used in § 3.5.2 for estimating the mass of the torus. We obtain that the total

mass of the molecular gas is 0.34, 0.8, or 1.85 $M_\odot$, depending on the values used for the preshock density. The mass is distributed as follows: $\sim 40\%$ of the mass is concentrated in the torus and $\sim 60\%$ in the ellipsoidal shells. For these shells we have assumed a shell thickness of 0.034 pc (obtained from the H$_2$ image). It is important to note that the mass corresponding to the torus differs from the value obtained in the above section; the reason is that in one case we have assumed a constant density, resulting in an upper limiting value. With this mass estimate we can suggest that probably the progenitor of NGC 2346 was a more massive star than the typical PN progenitors. Indeed, NGC 2346 is a type I PN; this fact and also its bipolar shape are in agreement with a massive progenitor. Corradi & Schwarz (1995) adopt a lower limit of 1.5 $M_\odot$ for the progenitors of bipolar PNs, although larger masses are also plausible, while on the contrary elliptical PNs are assumed to be formed by stars with $M \leq 1.1$ $M_\odot$. Because of the discussion given in § 3.5.2 we favored the intermediate value of 0.8 $M_\odot$. Thus, the mass estimate obtained in this work

corroborates that this bipolar and type I PN could have been formed by a more massive progenitor.

In obtaining this mass estimate we have assumed that the velocity of the red giant wind was the same at the torus and at the lobes. However, there is an actual debate about how bipolar nebulae are formed. In the case of isolated stars, the asymmetry that gives place to the bipolar shape is thought to be due to the ejection of an equatorial ring as a result of the star rotation or the presence of a bipolar magnetic field. Another possibility is a binary system in which one of the members transfers mass to the other so that an accretion disk is formed. In any case, the complex structure must be taken into account and perhaps it is not realistic to consider an isotropic red giant wind velocity. For example, Soker & Rappaport (2000) argued that nebulae with very narrow equatorial waists are generated by a two-winds interaction in a binary system: a slow wind blown by an asymptotic giant branch (AGB) star, and a collimated fast wind blown during the main-sequence or white dwarf phase of the companion. In this latter case, the collimated wind forms the lobes along the polar axis and compresses the slow wind near the equator. Since in the case of the lobes of NGC 2346 there is no CO velocity information, we adopted an isotropic red giant wind velocity. Red giant wind velocities larger at the lobes would imply smaller shock velocities and consequently larger preshock densities than those obtained in the isotropic case. Thus, the values obtained for the total mass of NGC3246 are only lower limits.

3.6. *Origin of the Emission*

Concerning the origin of the emission, shocks or PDRs, we know that if the emission is due to shocks, the line ratio $R(2–1/1–0)$ depends only on the shock velocity and has a maximum value of ~ 0.3 for strong shocks. In our direct images shown in Figure 2, the torus shows a line ratio with a maximum value of 0.15, suggesting a shock emission instead of PDRs, while the lobes have emission very close to the detection limit especially in the $S(1)$ 2–1 line; thus, we cannot derive any value of this ratio for the lobes. However, in the K-band spectra shown in Vicini et al. (1999), the $R(2–1/1–0)$ line ratio varies from 0.08 in the equatorial plane to 0.15 and 0.23 in the outer regions supporting the fact that, also for the lobes, the emission at these lines is due to shocks.

On the other hand, Vicini et al. (1999) concluded that the H_2 emission comes from a PDR in a low-density molecular shell. They used the models of Natta & Hollenbach (1998), which compute the emission originating in the PDR created at the inner edge of the neutral shell inside the precursor red giant wind. The models are time-dependent and take into account the effects of shocks, FUV radiation and soft X-rays. However, they have estimated the age of the nebula (2500 yr) by assuming an expansion velocity value of ~ 25 km s^{-1}, which is 10 km s^{-1} larger than our measured value. They have also assumed $V_{rg} = 8$ km s^{-1}. Using our measured expansion velocity, we derive a kinematic age of 3500 yr, and referring to Figure 4 of Vicini et al. (1999), we note that the observed H_2 $S(1)$ 1–0 intensity is better fitted by another of their models with a higher density ($n_0 \sim 2.1 \times 10^4$ cm^{-3}) than the model adopted by these authors ($n_0 \sim 7 \times 10^3$). Thus, the ambient density derived from the PDR models is larger than our limiting value of 1.7×10^4 cm^{-3} (obtained for ambient gas temperatures of 10 K), and consequently our determination of the kinematical age also

supports the conclusion that the 2.122 μm emission in NGC 2346 is due to shocks.

4. CONCLUSIONS

We have measured the velocity field of the molecular hydrogen gas in NGC 2346. The expansion velocity of the molecular gas at the central ring is 16 km s^{-1}, once it is deprojected by nebular inclination. For a torus radius of 17″ (0.057 pc) this implies a kinematic age of 3500 yr.

We have tested the predictions of several geometric models with our kinematic data and have selected a geometric model consisting of two ellipsoidal shells expanding radially with a velocity law $V \sim r$ and a density law $n \sim r^{-2}$.

We have estimated the preshock H_2 density from the 2.122 μm emission-line surface brightness and a shock velocity that depends on the value of the red giant velocity. Since this latter quantity is not very well known, we have assumed a set of three possible values that lead to three values of the preshock density: (0.3, 0.7, and 1.7) $\times 10^4$ cm^{-3}. The 3×10^3 cm^{-3} value, obtained for $V_{rg} = 0$ km s^{-1}, corresponds to the lower limiting value of the preshock density.

We compared this set of density values with the ones obtained from CO observations of the torus (Bachiller et al. 1989). We used the fact that the column density of CO observations is equally sensitive to both the density and the temperature to obtain an upper limit of the preshock density (1.7×10^4 cm^{-3}) corresponding to gas at $T = 10$ K, which is too low for a gas near a high-temperature star, and also corresponding to our density estimate by taking $V_{rg} = 10$ km s^{-1}. Thus, we conclude that the preshock density value should be intermediate between those limits, favoring a preshock density of about 7×10^3 cm^{-3}.

We have estimated the total molecular mass of the bipolar nebula by assuming a density law of r^{-2} and using the two-ellipsoidal shell geometric model. For the intermediate value of the preshock density considered, the molecular mass estimate is 0.8 $M_\odot$, which is much larger than the value 0.01 $M_\odot$ derived for the ionized gas. This new mass determination corroborates, in an independent way, that this bipolar, type I PN should have a more massive progenitor than the typical PNs. Note that H_2 and CO mass estimates depend on two unknown parameters: the velocity of the red giant envelope and the temperature of the preshock gas. Any attempt to measure these parameters should improve the accuracy of the mass determination.

Furthermore, according to our mass estimate and kinematic age, in agreement with typical AGB winds, we have derived a plausible value for the mass-loss rate, $\dot{M} \geq 5 \times 10^{-4}$ $M_\odot$ yr^{-1}.

We have given arguments to show that shocks are at the origin of the H_2 emission lines at 2.122 and 2.248 μm for this PN.

We have discussed that if shocks are at the origin of the H_2 emission it is important to recall that, in the case of J-type shocks, molecular dissociation occurs for shocks stronger than 25 km s^{-1}. However, our data are well-fitted to a model that predicts shock velocities larger than 50 km s^{-1} at the ends of the lobes. This could imply that C-type shocks and the presence of a magnetic field are more adequate to explain the kinematics of the H_2 gas that we observed. Another possibility is that the H_2 molecule is more robust than previously thought (Williams 2001).

REFERENCES

Anandarao, B. G., Banerjee, D. P. K., Desai, J. N., Jain, S. K., & Mallik, D. C. V. 1988, MNRAS, 235, 221
Bachiller, R., Planesas, P., Martín Pintado, J., Bujarrabal, V., & Tafalla, M. 1989, A&A, 210, 366
Balick, B. 1987, AJ, 94, 671
Black, J. H., & van Dishoeck, E. F. 1987, ApJ, 322, 412
Chu, Y. H., Jacoby, G. H., & Arendt, R. 1987, ApJS, 64, 529
Corradi, R. L. M., & Schwarz, H. E. 1995, A&A, 293, 871
Cruz-González, I., et al. 1994, Proc. SPIE, 2198, 774
Healy, A. P., & Huggins, P. J. 1988, AJ, 95, 866
Kastner, J. H., & Gatley, I. 2000, in ASP Conf. Ser. 199, Asymmetrical Planetary Nebulae II: From Origins to Microstructures, ed. J. H. Kastner, N. Soker, & S. A. Rappaport (San Francisco: ASP), 387
Kastner, J. H., Gatley, I., Merrill, K. M., Probst, R., & Weintraub, D. A. 1994, ApJ, 421, 600
Kastner, J. H., Weintraub, D. A., Gatley, I., Merrill, K. M., & Probst, R. G. 1996, ApJ, 462, 777
Knapp, G. R. 1986, ApJ, 311, 731
Kwan, J. 1977, ApJ, 216, 713
Latter, W. B., Kelly, D. M., Hora, J. L., & Lynne, K. D. 1995, ApJS, 100, 159
Le Coarer, E., Rosado, M., Georgelin, Y., Viale, A., & Goldes, G. 1993, A&A, 280, 365
Méndez, R. H. 1978, MNRAS, 185, 647

Méndez, R. H., Niemela, V. S., & Lee, P. 1978, MNRAS, 184, 351
Natta, A., & Hollenbach, D. 1998, A&A, 337, 517
Pascoli, G. 1990, A&A, 232, 184
Rosado, M. 1995, Rev. Mexicana Astron. Astrofis. Ser. Conf., 3, 268
Rosado, M., et al. 1999, in Proc. SPIE, 3354, 1111
Salas, L., et al. 1999, ApJ, 511, 822
Shull, J. M., & Hollenbach, D. J. 1978, ApJ, 220, 525
Soker, N., & Rappaport, S. 2000, ApJ, 538, 241
Sternberg, A., & Dalgarno, A. 1989, ApJ, 338, 197
Takami, M., Usuda, T., Sugai, H., Kawabata, H., Suto, H., & Tanaka, M. 2000, ApJ, 529, 268
Terzian, Y. 1997, in IAU Symp. 180, Planetary Nebulae, ed. H. J. Habing & H. J. G. L. M. Lamers (Dordrecht: Kluwer), 29
Treffers, R. T., Fink, U. F., Larson, P. L., & Gautier, N. T. 1976, ApJ, 209, 793
Vicini, B., Nata, A., Marconi, A., Testi, L., Hollenbach, D., & Draine, B. T. 1999, A&A, 342, 823
Walsh, J. R. 1983, MNRAS, 202, 303
Walsh, J. R., Meaburn, J., & Whitehead, M. J. 1991, A&A, 248, 613
Williams, D. 2001, in Rev. Mexicana Astron. Astrofis. Ser. Conf., Emission Lines fron Jet Flows, ed. Henney, W., Steffen, W., Binette, L., & Raga, A., in press
Zhang, C. Y., & Kwok, S. 1998, ApJS, 117, 341
Zuckerman, B., & Gatley, I. 1988, ApJ, 324, 501